Metasurface Enabled Wide-Angle Fourier Lens

Wenwei Liu, Zhancheng Li, Hua Cheng, Chengchun Tang, Junjie Li, Shuang Zhang,* Shuqi Chen,* and Jianguo Tian

Fourier optics, the principle of using Fourier transformation to understand the functionalities of optical elements, lies at the heart of modern optics, and it has been widely applied to optical information processing, imaging, holography, etc. While a simple thin lens is capable of resolving Fourier components of an arbitrary optical wavefront, its operation is limited to near normal light incidence, i.e., the paraxial approximation, which puts a severe constraint on the resolvable Fourier domain. As a result, high-order Fourier components are lost, resulting in extinction of high-resolution information of an image. Other high numerical aperture Fourier lenses usually suffer from the bulky size and costly designs. Here, a dielectric metasurface consisting of high-aspect-ratio silicon waveguide array is demonstrated experimentally, which is capable of performing 1D Fourier transform for a large incident angle range and a broad operating bandwidth. Thus, the device significantly expands the operational Fourier space, benefitting from the large numerical aperture and negligible angular dispersion at large incident angles. The Fourier metasurface will not only facilitate efficient manipulation of spatial spectrum of free-space optical wavefront, but also be readily integrated into micro-optical platforms due to its compact size.

Fourier optics represents an important platform for diverse applications such as spatial filtering,[1,2] compressed sensing,[3] and holography.[4–6] The basic building block of Fourier optics is

Dr. W. Liu, Dr. Z. Li, Prof. H. Cheng, Prof. S. Chen, Prof. J. Tian
The Key Laboratory of Weak Light Nonlinear Photonics
Ministry of Education
School of Physics and TEDA Institute of Applied Physics
Nankai University
Tianjin 300071, China
E-mail: schen@nankai.edu.cn
Prof. H. Cheng, Prof. S. Chen, Prof. J. Tian
The Collaborative Innovation Center of Extreme Optics
Shanxi University
Taiyuan, Shanxi 030006, China
Dr. C. Tang, Prof. J. Li
Beijing National Laboratory for Condensed Matter Physics
Institute of Physics
Chinese Academy of Sciences
Beijing 100190, China
Prof. S. Zhang
School of Physics and Astronomy
University of Birmingham
Birmingham B15 2TT, UK
E-mail: s.zhang@bham.ac.uk

Fourier lens, which can perform a Fourier transform of the incident wavefront at the focal plane.[7] Traditional Fourier lens is realized by a thin transparent medium with slowly varying thickness that can accumulate optical phase under the paraxial approximation. This approximation greatly restricted the ability of Fourier lens to resolve a large k component of a wavefront. Another way to produce a Fourier lens is employing diffractive methods such as holography to realize a convenient phase design.[8] However, these traditional Fourier lenses are very challenging to manufacture with high precision, especially those working with large field-of-view.

In recent years, the burgeoning field of metasurfaces provides a high degree of freedom for locally tailoring the optical properties on subwavelength scale based on plasmonic[9–18] and dielectric building blocks.[19–24] Complete control over the phase and polarization of light has been achieved via waveguide based metasurfaces.[25–27] With delicate design of phase distribution, 3D holography,[28,29] multiwavelength achromatic holography,[30] and nonlinear holography[31] have also been accomplished. Metasurfaces can be designed to operate as flat lenses, the so-called metalens. With a tailored hyperbolic phase distribution, metalens can convert a plane wavefront to a spherical one.[32–35] This method has been applied to cancel chromatic aberration in the infrared waveband[36,37] and the visible regime[38] via judicious phase design. It is also demonstrated that metalens can replace conventional objectives for subwavelength resolution imaging.[39] Subdiffraction light focusing has also been demonstrated with plasmonic metalens by employing superoscillatory behavior beyond the Abbe diffraction limit.[40] Recently, a doublet corrected metalens is proposed to achieve monochromatic aberrations with an incident angle reaching 30°,[41] which is approaching the boundary of the paraxial approximation ($\sin \pi/6 \approx \pi/6$). However, the abovementioned metalenses are designed for imaging and cannot be utilized to perform Fourier transform when the incident angle is greater than 30°. To the best of our knowledge, none of the previous works on Fourier lenses is able to work beyond 30° with applicable efficiency.[42] Here, we demonstrate a 1D Fourier metalens made of an array of dielectric waveguide resonators, which shows good performance for 0–60° of incidence angle covering a broad bandwidth from 1100 to 1700 nm. The superior performance of the metalens
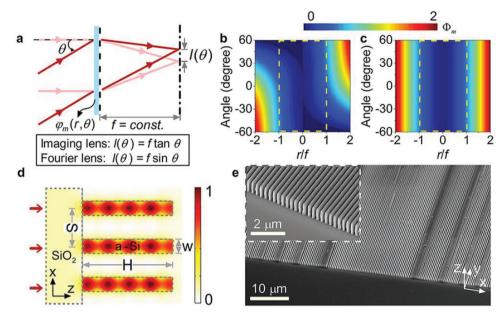
Figure 1. Design and fabrication of the Fourier metalenses. a) With an incident angle of θ, the focal spot will move a distance of $l(\theta)$ along the focal plane. b) The required phase delay against positions of the nanostructures and the incident angle, where $l(\theta) = f\sin\theta$ (Fourier lenses). c) The angle-dispersion-free phase delay with a first order approximation before compensation of initial phase, against positions of the nanostructures and the incident angle. The yellow dashed boxes in (b) and (c) indicate the areas used in the fabricated Fourier lens. d) Schematic of the Fourier metalens and its building block with magnetic intensity distribution. The amorphous silicon (a-Si) nanolines are designed with: $H = 1050$, $S = 450$ nm. e) SEM micrograph of the fabricated Fourier metalens.

is confirmed through the Fourier transform/Fraunhofer diffraction of a grating with periodicity slightly greater than the wavelength. The platform we propose does not suffer from the paraxial approximation and provides a powerful framework for realizing optical Fourier operation.

A generic illustration of the light path for oblique focusing of monochromatic light is shown in **Figure 1**a. The coupling efficiency from air to the metasurface is generally lower than that from substrate to the metasurface, especially for oblique incidence, which may lead to discrepancy between the element simulation and the device simulation.[43] Thus, the incident light travels through the air onto the substrate of the metasurface in our setup. Each incident angle θ corresponds to a focus in the focal plane, with an foci offset of $l(\theta)$ from the origin, which is called spatial frequency in Fourier optics. To achieve the desired focusing functionality, an abrupt phase shift ϕ_m is required along the surface of the metasurface to compensate the phase accumulated via propagation. Since ϕ_m is inversely proportional to the operating wavelength,[32] a better way to express ϕ_m is to normalize it by $k_0 f$

$$\Phi_m(r,\theta) = \gamma\sin\theta + \sqrt{1 + \left(\gamma - \frac{l(\theta)}{f}\right)^2} - \sqrt{1 + \left(\frac{l(\theta)}{f}\right)^2} \quad (1)$$

where $\Phi_m(r,\theta) = -\phi_m/k_0 f$, $\gamma = r/f$, k_0 is the wavevector of the incident wave, f is the focal length, and r is the coordinate along the surface of the lens. When θ and $l(\theta)$ approach zero, Equation (1) recovers the hyperbolic formula working in normal incidence. For a Fourier lens, $l(\theta) = f\sin\theta$ is required, and the corresponding phase shift Φ_m is computed via Equation (1) and shown in Figure 1b. Recently, a 2D plasmonic wide-angle flat

lens that can realize $l(\theta) = f\sin\theta$ in the visible has been proposed,[44] which opened up the possibility of realizing large field-of-view as Fourier transformation devices at micro scale. With an incident angle above 30° and position $|r/f| > 1$, Φ_m is highly angle-dispersive, which hinders the development of large-angle Fourier lenses.

As a comparison, the foci offset for an imaging lens is $l(\theta) = f\tan\theta$ (see Figure S1 in the Supporting Information). Thus, the existing high numerical aperture lenses with large field-of-view[39,41] are not applicable as Fourier lenses. Another type of lens for manipulating the focal plane is F-theta scan lens with $l(\theta) = f\theta$, which is often used in carving systems and scanning systems. Commercial F-theta scan lenses are usually designed to work at small incident angles, such as Thorlabs FTH100 (±28°), because Φ_m is also highly angle-dispersive for large incident angles. Generally, an artificial design of $l(\theta)$ is required to match various needs of manipulating the focal plane. Here, we demonstrate a Fourier metalens breaking the paraxial condition based on dielectric waveguides (DWs). By applying a Taylor series $(1 + x)^a \approx 1 + ax$ to the first order, Equation (1) can be simplified as

$$\Phi_m(r,\theta) \approx \gamma\sin\theta + \frac{1}{2}\gamma^2 - \frac{\gamma l(\theta)}{f} \quad (2)$$

Substituting $l(\theta) = f\sin\theta$ into Equation (2), we obtain $\Phi_m(r,\theta) \approx \gamma^2/2$, which is angle-dispersion-free (Figure 1c). It should be noticed that this phase distribution is only for theoretical analysis and generally is difficult to be realized by most of the optical materials especially for those plasmonic antennas whose resonance frequency changes with varied incident angles.[45] To solve this problem, a compensation of initial phase
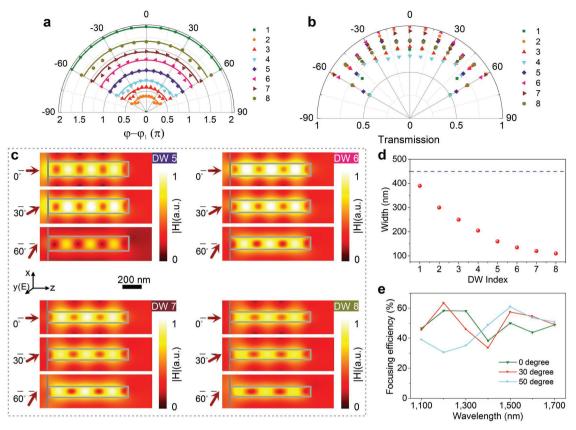
Figure 2. Theoretically realizing the Fourier metalens. a) Simulated phase difference $\phi-\phi_1$ (dots) for selected eight DWs under −60° to 60° incidence, where ϕ is the phase of each DW, and ϕ_1 is the phase of the first DW. The solid lines are eye guides. b) Simulated transmission of each DW under −60° to 60° incidence. All of the transmissions are larger than 0.5, and have an average value at around 0.8. The incident wavelength in (a) and (b) is 1550 nm. c) Simulated magnetic field intensity (1550 nm) when light propagates at 0°, 30°, and 60°, respectively. d) Eight widths of the nanolines (red dots) in the simulation and experiments. All of these widths are smaller than the size of the unit cell (blue dashed line) by at least 60 nm to avoid adhesion of DWs. e) Simulated focusing efficiency as a function of wavelength. This efficiency is defined as the fraction of the incident optical power that is converted to the transmitted focusing light.

is required. Since it is the phase difference that determines the wavefront of output light rather than the absolute phase value, the phase equation can be generalized as

$$\Phi'_m(r,\theta) = \Phi_m(r,\theta) - \Phi(0,\theta) \quad (3)$$

where $\Phi(0,\theta)$ is the phase at $r = 0$ under an oblique incident angle θ. As demonstrated in the following part, the phase distribution Φ'_m can be realized with elaborate design of DWs. The term $\Phi(0,\theta)$ relaxes the constraint in Equation (2) and simplifies the realization of an angle-dispersion-free phase distribution, enabling the DWs we designed to function in a large range of incident angles (see Figures S7–S9 in the Supporting Information).

To achieve the desired phase distribution, we designed DWs of amorphous silicon (a-Si) on fused silica substrate, with a height of $H = 1050$ nm and a lattice size of $S = 450$ nm (Figure 1d). Figure 1e shows the scanning electron microscope (SEM) images of the metalens fabricated using the a-Si DWs. The size of the designed Fourier metalens is 190 × 100 µm (190 µm along x-direction). We select eight widths of DWs using a commercial finite element method-based COMSOL

Multiphysics software[46] (**Figure 2**). Permittivity of a-Si used in the simulation is taken from ref. [47], and the incident polarization is along y-direction (TE incidence). Since the metalens is homogeneous along y-direction, the incident wave vector maintains in x–z plane, and the incident angle is defined as the intersection angle between wave vector and z-axis in our setup. The simulated phase difference $\phi-\phi_1$ at 1550 nm is shown in Figure 2a, where ϕ_1 is the phase of the DW 1 (Figure 2d). According to the simulation, the eight DWs have a phase variation in the whole range 0–2π, and the phase variation for each DW is less than 0.164 π under 0–60° incidence. This phase profile satisfies Equation (3) for achieving Fourier operation. The simulated transmission $|t|$ is around 0.8, and the minimum $|t|$ is over 0.5 (Figure 2b). Taking the fifth to eighth DWs as an example, we simulated the waveguide modes (magnetic intensity distribution) of the DWs under 1550 nm incidence in Figure 2c. The weak waveguide response of DW 5 with 60° incidence is still similar to those with 0° and 30° incidence. The optimal element DW 7 can maintain a transmission higher than 0.85 for 0–60° incidence. The simulated magnetic field intensities with incident angle θ of 0°, 30°, and 60° show that light is mainly confined inside the high-refractive-index DWs,
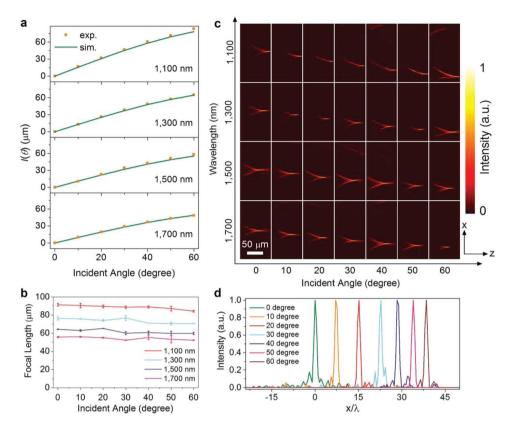
Figure 3. Experimental demonstration of the Fourier metalens with incline incidence. a,b) Measured and simulated (a) foci offset $l(\theta)$ and (b) focal length with different incident wavelengths and angles. c) Intensity distribution of the x–z plane, showing the evolution of the foci offset $l(\theta)$ for different incident angles and wavelengths. d) Measured focusing vertical cut (1500 nm) at 0° to 60° incidence.

with negligible coupling between the neighboring DWs, and the scattered light is primarily determined by the transmission and phase of each DW.[48] Furthermore, the waveguide mode remains nearly the same under different incident angles, i.e., the angle-dispersion-free performance is satisfied. In a simplified picture, each DW can be treated as a low-quality-factor Fabry–Pérot resonator, with the effective refractive indices of the waveguide determined by the width of the waveguide. To statistically quantify the fluctuation of the phase-change for different incident angles, we calculated the standard deviation (STD)

of the phase factor $s_i = e^{-i(\varphi_i - \varphi_1)}$ with $\text{STD} = \sqrt{\dfrac{1}{N}\sum_{i=1}^{N}| s_i - \overline{s} |^2}$,

as shown in Figure S12 in the Supporting Information. The highest STD of the phase factor of the phase-change occurs in the waveband around 1100 nm, which indicates a relatively higher fluctuation of phase-change. This fluctuation leads to acceptable aberrations in the focal plane, which can be observed in the experimental results in **Figure 3**c. Thus, the required control of phase can be achieved through optimizing the width of DWs, and transmission is determined by the quality-factor of the waveguide. Simulations in Figure 2e show that focusing efficiencies as high as ≈50% are achieved through the waveband of 1100–1700 nm. The size of the simulated metalens is the same as the fabricated sample with the focal length set as 74.5 µm for 1300 nm incidence. The focusing efficiency is calculated as the ratio of focused power to the total incident optical

power. To exclude the transmitted background light which affects the accuracy of the calculated efficiency, we set a line probe with 50 µm width in the focal plane. Then, we integrated the light energy of the line probe and divided it by the power of the incident optical beam. The bandwidth of the element in our study originates from the waveguide mode of DWs. The phase modulation of DWs follows the formula $\varphi_{DW} = 2\pi n_{eff} H / \lambda_d$, and is usually functions through a broad waveband.[49] The calculated group delay of DW 7 is around 30 fs with fluctuation of 5 fs (see Figure S13 in the Supporting Information), which quantitatively demonstrates the broadband behavior of the building blocks.[50]

As shown in Figure 3a, the measured foci offset $l(\theta)$ shows a good agreement with the theoretical one: $l(\theta) = f \sin\theta$ across a broad bandwidth. The measured focal length as a function of incident angles for different incident wavelengths is shown in Figure 3b. Since the metalens has a chromatic dispersion, the focal length decreases as the wavelength increases. Importantly, there is no field curvature in the focal plane since the focal length remains almost the same with varied incident angles. This characteristic fits the design schematic shown in Figure 1a, consequently the focal plane is a flat rather than a curved surface, which facilitates the spatial filtering process in applications of Fourier optics.[7] As shown in Figure S10 (Supporting Information), the simulated focal lengths remain the same for 0–60° incidence. In addition, we measure the beam intensity profile of the metalens in the x–z cross-section (Figure 3c), showing
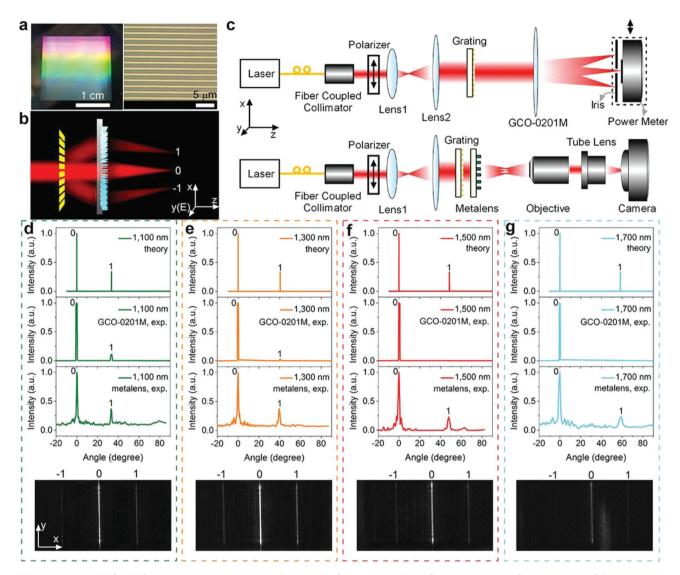
Figure 4. Fourier transform of a grating by the metalens. a) Photograph of the grating under a fluorescent lamp (left). Photograph of the grating taken by a CCD camera (right). The grating has a period of 2 µm, and duty cycle of 0.45. b) Schematic of the Fourier transform via the metalens. c) Illustration of the measurement set-up for the Fourier transform through a commercial Fourier lens GCO-0201M (top) and the metalens (bottom). d–g), Fourier transform in the focal plane at wavelengths of (d) 1100 nm, (e) 1300 nm, (f) 1500 nm, and (g) 1700 nm. Top (d–g): The 0th and 1st order diffraction according to the theoretical calculation and the corresponding measurement through GCO-0201M and the metalens. Bottom (d–g): photographs of the Fourier-transformed focal plane through the metalens taken by an InGaAs camera.

the evolution of the foci offset $l(\theta)$ for different incident wavelengths and angles. The weak noises in the profiles are caused by the bright field image of incident light, which, nonetheless, does not affect the measurement of $l(\theta)$ and focal length. The spherical aberrations observed are due to the parabolic phase distribution, and can be removed by using a corrector plate placed at the aperture stop of the lens,[42] which is beyond the current scope of this study. The intensity profiles of the vertical cuts of the focal lines for 1500 nm is shown in Figure 3d. For 0–60° incidence, full width at half maximum is about λ and an evident shift is observed along x-axis when increasing the incident angle. The designed Fourier metalens can still work for different incident polarization states (see Figure S11 in the Supporting Information). However, the efficiency for TM incidence is lower than that for TE incidence. The efficiency can

reach maximum value under y-polarized incidence. We did not directly measure the focusing efficiency of the metalens in the experiment, since a long working distance objective with the numerical aperture (NA) of at least 0.93 is required. The highest NA of the commercial objective with long working distance suitable for this waveband (1100–1700 nm) is usually below 0.8.

It should be mentioned that $l(\theta) = f \sin \theta$ is a necessary but not a sufficient condition to realize a Fourier lens, since one must take intensity into consideration. To demonstrate the Fourier transform ability of the metalens, we design a transmission grating as shown in **Figure 4**a. The grating constant is 2 µm, allowing 0th and ± 1st order of Fraunhofer diffraction from 1100 to 1700 nm.[7] The schematic of the Fourier transform process is shown in Figure 4b. Since the grating is a dispersive
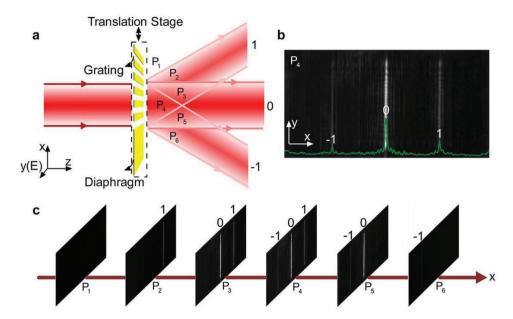
ADVANCED
SCIENCE NEWS
www.advancedsciencenews.com

ADVANCED
MATERIALS
www.advmat.de

Figure 5. Spatial filtering of the Fourier metalens in the focal plane. a) Schematic of the filtering process. By moving the grating along the *x*-axis through a translation stage, the metalens will locate at the positions of P_1–P_6, and the metalens will transform the incident light to various spatial spectra. b) Intensity distribution in the focal plane for 1300 nm incidence with the metalens at P_4, where no spatial filtering occurs. c) Intensity distribution with the metalens located at the positions of P_1–P_6 (1300 nm). The diffraction orders of −1, 0, 1 in sequence arise and vanish, mimicking spatial filtering through a rejector.

device, the longer the incident wavelength is, the larger the diffraction angle will be. The diffraction angle is characterized by using the set-up shown in Figure 4c. The grating is illuminated by *γ*-polarized light, and the diffraction field is Fourier-transformed by a commercial Fourier lens and the metalens, respectively. As shown in the top row of Figure 4d–g, the theoretical calculated divergent angle of the 1st order diffraction is 33.4° for 1100 nm, 40.5° for 1300 nm, 48.6° for 1500 nm, and 58.2° for 1700 nm, respectively. When using the metalens to perform the Fourier transform, the measured angles of the 1st order diffraction are 33.0° for 1100 nm, 39.4° for 1300 nm, 48.0° for 1500 nm, and 59.0° for 1700 nm, which show a good agreement with the theoretical calculation. In comparison, as the commercial Fourier lens is designed under the paraxial approximation, it cannot work for large incident angles (larger than 30°). Although the commercial Fourier lens can exhibit the 1st order diffraction for the wavelengths of 1100 and 1300 nm, which is 33.0° and 40.0°, respectively, the intensity of the 1st order diffraction is about an order of magnitude less than the theoretical ones. Whereas the measured intensities of the 1st order diffraction by the metalens are very close to the theoretical ones. The measured Fraunhofer diffraction spectra are obtained by $\theta = \arcsin(z/f)$, where z is the z-coordinate of the captured field profile in the focal plane, and f is the measured focal length. The measured diffraction peaks are broader than the calculated ones, which can be attributed to the limited size of the grating and efficiency of the metalens. The captured intensity profiles by an InGaAs camera in the focal plane are shown in the bottom row of Figure 4d–g, displaying 0th and ± 1st order diffraction for each incident wavelength. Furthermore, we demonstrate spatial filtering using the grating and the metalens (1300 nm). The grating is fabricated with an Au

diaphragm on a silica substrate. By moving the grating along *x*-direction through a translation stage, the Au diaphragm gradually blocks more and more incident beams, and the metalens is illuminated in different positions from P_1 to P_6, as shown in **Figure 5**a. Taking P_3 as an example, the metalens is illuminated by the 0th and 1st order diffraction, with the 1st order being filtered out. The intensity distribution without spatial filtering is shown in Figure 5b, and the filtering process from P_1 to P_6 can be seen in Figure 5c. The change in the recorded pattern with moving the grating is shown in Movies S1–4 (Supporting Information) for different incident wavelengths (1100, 1300, 1500, and 1700 nm). The spatial filtering results further confirm that the designed Fourier metalens is capable of performing Fourier transform of the incident wavefront at large incident angles.

Our work demonstrates that, through the coupling of the incident light with DW resonators, a near angle-dispersion-free phase change can be achieved. By choosing the widths of DWs, a Fourier metalens allowing large incident angles is demonstrated and agrees well with the theoretical predictions. Considering the broadband behavior, our metalens is compatible with commonly used telecommunication platform, could be readily integrated into micro-optical platforms, and could directly replace conventional thin lenses. It should be noticed that the methodology proposed in this study are not limited to Fourier lenses. The starting point is that we can manipulate the positions of the foci in the focal plane to transform image or information, taking advantages of the considerable ability of metasurfaces to arbitrarily control amplitude, phase, and polarization. Since focusing also means magnifying the energy density a lot, this method may benefits information transmission in nonlinear optics. We note that the theoretical approach and the design technique can be simply introduced

**ADVANCED
SCIENCE NEWS**

www.advancedsciencenews.com

**ADVANCED
MATERIALS**

www.advmat.de

to similar platforms, such as titanium dioxide based metalens in the visible wavelengths.[51] This approach can also be extended to 2D or 3D Fourier devices to exhibit a full reciprocal lattice in *k*-space, which introduces more degrees of freedom for describing arbitrary electromagnetic waves, such as Bessel beams and Airy beams.

Experimental Section

Sample Fabrication: The metalens were fabricated on a fused silica substrate. First, a layer of 1050 nm amorphous silicon was coated on the substrate with plasma enhanced chemical vapor deposition method. Then, a layer of polymethyl methacrylate (PMMA) with thickness of 200 nm and a layer of Pedot:PSS with thickness of 35 nm were spun coated on the substrate by sequence. The Pedot:PSS layer was intended for charge release during the electron-beam lithography (EBL) process which employed a 100 kV voltage, 200 pA current, and 1000 μC cm^{-2} dose. After the EBL process, the Pedot:PSS layer was removed with pure water for 60 s and PMMA was developed with MIKE\IPA(3:1) for 40 s. Then, a 50 nm Cr layer was deposited on the resist with electron beam evaporation deposition method. Then, the Cr film was striped by removing PMMA with hot acetone at degree of 60 °C for 20 min, which was followed by HBr plasma dry etching with inductively coupled plasma (ICP) machine. The residue Cr resist was removed by wet etching method. Finally, 3 nm Cr layer was coated for SEM and then removed with wet etching method before optical measurement.

Measurement Procedure: The measurements of the focusing are based on a home-built microscopy as shown in Figure S6a in the Supporting Information. The light source was a supercontinuous laser (NKT SuperK EXR-20), and the laser beam was collimated by a fiber collimator. Then the collimated beam passed through an infrared polarizer, and the output light from the sample was collected with an objective (Sigma NIR plan apo 50×, NA = 0.67), a tube lens (Thorlabs TL200-3P), and an InGaAs camera (HAMAMATSU InGaAs C10633). The objective, tube lens, and InGaAs camera were all integrated on a *XYZ* translation stage to scan the focusing profile of the metalens. The measurements diffraction were accomplished with the optical setup in Figure 4c. A pair of lenses (focal length of 30 and 150 mm) was used to magnify the beam diameter up to ≈5 mm, making the light diffracted by the grating illuminate the sample for all incident wavelengths. The grating was placed in front of the metalens with a distance of ≈1 mm. With a normal incidence, the photography was captured in the focal plane with the InGaAs camera. The spatial filtering measurement was via moving the grating along *x*-axis through a translation stage. A commercial Fourier lens GCO-0201M (*f* = 300 mm) was used to compare with metalens. A power meter (Thorlabs S132C) mounted with an iris was located at the focal plane of the Fourier lens. The diffraction angle was calculated through arcsin(z/f), where z was the measured position of the power meter and f was the focal length.

Supporting Information

Supporting Information is available from the Wiley Online Library or from the author.

Acknowledgements

Conflict of Interest

The authors declare no conflict of interest.

Keywords

[1] J. W. Goodman, *Introduction to Fourier Optics*, Roberts and Company Publishers, Greenwood Village, CO **2005**.
[2] A. V. Lugt, *IEEE Trans. Inf. Theory* **1964**, *10*, 139.
[3] D. L. Donoho, *IEEE Trans. Inf. Theory* **2006**, *52*, 1289.
[4] I. Yamaguchi, T. Zhang, *Opt. Lett.* **1997**, *22*, 1268.
[5] S. Eisebitt, J. Lüning, W. F. Schlotter, M. Lörgen, O. Hellwig, W. Eberhardt, J. Stöhr, *Nature* **2004**, *432*, 885.
[6] D. Gabor, *Nature* **1948**, *161*, 777.
[7] B. E. A. Saleh, M. C. Teich, *Fundamentals of Photonics*, Wiley, NY **1991**.
[8] A. M. Tai, M. T. Eismann, B. D. Neagle, *Opt. Eng.* **1993**, *32*, 3254.
[9] N. Yu, P. Genevet, M. A. Kats, F. Aieta, J. P. Tetienne, F. Capasso, Z. Gaburro, *Science* **2011**, *334*, 333.
[10] H. Cheng, S. Chen, P. Yu, X. Duan, B. Xie, J. Tian, *Appl. Phys. Lett.* **2013**, *103*, 203112.
[11] W. Liu, S. Chen, Z. Li, H. Cheng, P. Yu, J. Li, J. Tian, *Opt. Lett.* **2015**, *40*, 3185.
[12] Z. Liu, Z. Li, Z. Liu, J. Li, H. Cheng, P. Yu, W. Liu, C. Tang, C. Gu, J. Li, S. Chen, J. Tian, *Adv. Funct. Mater.* **2015**, *25*, 5428.
[13] X. Ding, F. Monticone, K. Zhang, L. Zhang, D. Gao, S. N. Burokur, A. Lustrac, Q. Wu, C.-W. Qiu, A. Alù, *Adv. Mater.* **2015**, *27*, 1195.
[14] A. Pors, M. G. Nielsen, R. L. Eriksen, S. I. Bozhevolnyi, *Nano Lett.* **2013**, *13*, 829.
[15] N. Meinzer, W. L. Barnes, I. R. Hooper, *Nat. Photonics* **2014**, *8*, 889.
[16] H. Cheng, Z. Liu, S. Chen, J. Tian, *Adv. Mater.* **2015**, *27*, 5410.
[17] P. Yu, J. Li, C. Tang, H. Cheng, Z. Liu, Z. Li, Z. Liu, C. Gu, J. Li, S. Chen, J. Tian, *Light: Sci. Appl.* **2016**, *5*, e16096.
[18] M. Pu, X. Li, X. Ma, Y. Wang, Z. Zhao, C. Wang, C. Hu, P. Gao, C. Huang, H. Ren, X. Li, F. Qin, J. Yang, M. Gu, M. Hong, X. Luo, *Sci. Adv.* **2015**, *1*, e1500396.
[19] D. Lin, P. Fan, E. Hasman, M. L. Brongersma, *Science* **2014**, *345*, 298.
[20] J. Bar-David, L. Stern, U. Levy, *Nano Lett.* **2017**, *17*, 1127.
[21] S. Jahani, Z. Jacob, *Nat. Nanotechnol.* **2016**, *11*, 23.
[22] Y. Yang, I. I. Kravchenko, D. P. Briggs, J. Valentine, *Nat. Commun.* **2014**, *5*, 5753.
[23] J. Cheng, D. Ansari-Oghol-Beig, H. Mosallaei, *Opt. Lett.* **2014**, *39*, 6285.
[24] A. Forouzmand, H. Mosallaei, *Adv. Opt. Mater.* **2017**, *5*, 1700147.
[25] J. Li, S. Chen, H. Yang, J. Li, P. Yu, H. Cheng, C. Gu, H. -T. Chen, J. Tian, *Adv. Funct. Mater.* **2015**, *25*, 5428.
[26] P. Yu, S. Chen, J. Li, H. Cheng, Z. Li, W. Liu, B. Xie, Z. Liu, J. Tian, *Opt. Lett.* **2015**, *40*, 3229.
[27] A. Arbabi, Y. Horie, M. Bagheri, A. Faraon, *Nat. Nanotechnol.* **2015**, *10*, 937.

**ADVANCED
SCIENCE NEWS**

www.advancedsciencenews.com

**ADVANCED
MATERIALS**

www.advmat.de

[28] L. Huang, X. Chen, H. Mühlenbernd, H. Zhang, S. Chen, B. Bai, Q. Tan, G. Jin, K.-W. Cheah, C.-W. Qiu, J. Li, T. Zentgraf, S. Zhang, *Nat. Commun.* **2013**, *4*, 2808.

[29] X. Li, L. Chen, Y. Li, X. Zhang, M. Pu, Z. Zhao, X. Ma, Y. Wang, M. Hong, X. Luo, *Sci. Adv.* **2016**, *2*, e1601102.

[30] B. Wang, F. Dong, Q.-T. Li, D. Yang, C. Sun, J. Chen, Z. Song, L. Xu, W. Chu, Y.-F. Xiao, Q. Gong, Y. Li, *Nano Lett.* **2016**, *16*, 5235.

[31] W. Ye, F. Zeuner, X. Li, B. Reineke, S. He, C.-W. Qiu, J. Liu, Y. Wang, S. Zhang, T. Zentgraf, *Nat. Commun.* **2016**, *7*, 11930.

[32] F. Aieta, P. Genevet, M. A. Kats, N. Yu, R. Blanchard, Z. Gaburro, F. Capasso, *Nano Lett.* **2012**, *12*, 4932.

[33] X. Ni, S. Ishii, A. V. Kildishev, V. M. Shalaev, *Light: Sci. Appl.* **2013**, *2*, e72.

[34] A. Arbabi, Y. Horie, A. J. Ball, M. Bagheri, A. Faraon, *Nat. Commun.* **2015**, *6*, 7069.

[35] X. Chen, L. Huang, H. Mühlenbernd, G. Li, B. Bai, Q. Tan, G. Jin, C.-W. Qiu, S. Zhang, T. Zentgraf, *Nat. Commun.* **2012**, *3*, 1198.

[36] M. Khorasaninejad, F. Aieta, P. Kanhaiya, M. A. Kats, P. Genevet, D. Rousso, F. Capasso, *Nano Lett.* **2015**, *15*, 5358.

[37] F. Aieta, M. A. Kats, P. Genevet, F. Capasso, *Science* **2015**, *347*, 1342.

[38] M. Khorasaninejad, Z. Shi, A. Y. Zhu, W. T. Chen, V. Sanjeev, A. Zaidi, F. Capasso, *Nano Lett.* **2017**, *17*, 1819.

[39] M. Khorasaninejad, W. T. Chen, R. C. Devlin, J. Oh, A. Y. Zhu, F. Capasso, *Science* **2016**, *352*, 1190.

[40] D. Tang, C. Wang, Z. Zhao, Y. Wang, M. Pu, X. Li, P. Gao, X. Luo, *Laser Photonics Rev.* **2015**, *9*, 713.

[41] A. Arbabi, E. Arbabi, S. M. Kamali, Y. Horie, S. Han, A. Faraon, *Nat. Commun.* **2016**, *7*, 13682.

[42] D. A. Buralli, G. M. Morris, *Appl. Opt.* **1989**, *28*, 3950.

[43] J. Cheng, S. Jafar-Zanjani, H. Mosallaei, *Sci. Rep.* **2016**, *6*, 38440.

[44] M. Pu, X. Li, Y. Guo, X. Ma, X. Luo, *Opt. Express* **2017**, *25*, 31471.

[45] J. Y. Yin, X. Wan, Q. Zhang, T. J. Cui, *Sci. Rep.* **2015**, *5*, 12476.

[46] *COMSOL Multiphysics User's Guide, Version 3.5*, Comsol AB, Burlington, MA **2008**.

[47] E. D. Palik, *Handbook of Optical Constants of Solids*, Academics Press, NY **1998**.

[48] W. Liu, Z. Li, H. Cheng, S. Chen, J. Tian, *Phys. Rev. Appl.* **2017**, *8*, 014012.

[49] M. Khorasaninejad, A. Y. Zhu, C. Roques-Carmes, W. T. Chen, J. Oh, I. Mishra, R. C. Devlin, F. Capasso, *Nano Lett.* **2016**, *16*, 7229.

[50] J. Cheng, H. Mosallaei, *J. Opt. Soc. Am. B* **2015**, *32*, 2115.

[51] R. C. Devlin, M. Khorasaninejad, W. T. Chen, J. Oh, F. Capasso, *Proc. Natl. Acad. Sci. USA* **2016**, *113*, 10473.